Science Robotics
AAAS

robotics.sciencemag.org/cgi/content/full/5/48/eabc8191/DC1

Supplementary Materials for

An agglutinate magnetic spray transforms inanimate objects into millirobots for biomedical applications

Xiong Yang, Wanfeng Shang, Haojian Lu, Yanting Liu, Liu Yang, Rong Tan, Xinyu Wu*, Yajing Shen*

*Corresponding author. Email: xy.wu@siat.ac.cn (X.W.); yajishen@cityu.edu.hk (Y.S.)

Published 18 November 2020, *Sci. Robot.* **5**, eabc8191 (2020)
DOI: 10.1126/scirobotics.abc8191

The PDF file includes:

Table S3. The swelling and disintegration time of cured film composed of different materials without magnetic oscillation.
Table S4. Substrates used in the M-skin disintegration testing.
Legends for movies S1 to S7
References (*36*, *37*)

Other Supplementary Material for this manuscript includes the following:

(available at robotics.sciencemag.org/cgi/content/full/5/48/eabc8191/DC1)

Movie S1 (.mp4 format). Coating of the M-spray droplet on target surfaces.
Movie S2 (.mp4 format). M-spray–enabled M-skin millirobots.
Movie S3 (.mp4 format). The environment adaptability of constructed M-skin millirobots.
Movie S4 (.mp4 format). Topology order reprogramming of the M-skin millirobot.
Movie S5 (.mp4 format). Magnetic-induced disintegration.
Movie S6 (.mp4 format). M-skin–covered catheter for active navigating.
Movie S7 (.mp4 format). M-skin–covered capsule for target drug delivery.

Supplementary materials

Supplementary text

The coating process of M-spray

A pressurization watering can is adopted to coat the M-spray on the target surface. Accompanies by high-speed airflow, the composite material is atomized into droplets, which size from 200 to 1000 μm and are coated towards the target inanimate object with a speed of ~1 m/s (Fig. 1B). The adhesion process of the single droplet on the target surface is shown in Fig. 1C. At the first stage, the droplet falls and causes deformation due to the impacting. Since the M-spray's self-adhesiveness, the landing droplet can stick on the surface firmly without bounce or lateral displacement, which makes the M-spray coating reliable. At the second stage, the droplet releases impact energy and restore shape within about 30 ms. During which, its shape changes into hemisphere while keeping the radius of the contact area unchanged. After that, the droplet approaches to steady state at the third stage. For the poor wettability PDMS, the shape of droplet and the radius of the contact area is hardly changed. For the hydrophilized glass with good wettability, the droplet spreads out slowly, and the radius of contact area increases at last. Here, no matter on what kinds of the target surface, the adhesion of the M-spray droplet is stable, and the contact area never decreases, which enabled the coating on diverse inanimate objects.

The colloid-solid transition of M-spray

To investigate the relationship between the transition rate and environment temperature, we daub quantitative M-spray (100 μL) with same component proportions (i.e., 40%

MPs content, 10% PVA solution concentration, 5% gluten content) to a rectangular plane (10 mm by 20 mm) under the same relative environment humidity 50%, and then thermal curing at different temperatures (30℃,50℃ and 70℃). The weight changing of M-spray during the whole curing process is recorded by balance scales (Sartorius ENTRIS224-1S) which reflect the colloid-solid transition rate of M-spray. To investigate the relationship between the M-skin thickness and material component proportions, quantitative M-spray (100 μL) with different component proportions (i.e., 30 to 50% MPs content, 5 to 15% PVA solution concentration) is coated to a rectangular plane (10 mm by 20 mm) and cures under the same temperature of 70℃ for 30 min.

Influences of raw material proportion on the M-skin

The M-skin is composited from PVA, gluten and MPs. During which, the PVA endows the M-spray self-adhesive and film-forming ability. Therefore, too little PVA solution concentration (<5%) will result in adhesive failure, and too large PVA solution concentration (>20%) will hinder droplet formation. The function of gluten is mainly to enhance the mechanical property of M-skin. Hence, the lower mass fraction of gluten will result in the flabby structure and faster disintegration of M-skin, while the too much gluten (higher than 10%) will generate agglomeration and hinder the atomization of M-spray. The M-spray has a higher tolerance for the MP mass fraction changing since the viscosity of raw material isn't sensitive to the MPs. However, the actuation ability of M-skin is positively proportional to the MPs mass fraction because iron is the only magnetic material in the raw materials. By weighing the fabrication, adhesiveness, actuation as well as reliability of M-skin, we used the PVA solution with a concentration of 10%, gluten with a mass fraction of 5% and MP with a mass fraction of 40% in experiments.

The brinell hardness test of M-skin

Hysitron Ubi-1 Nanoindenter detects the hardness of cured M-skin. The detect head first loaded gradually until reaching the max setting force 5000 μN and remain this state for 5 s following by unloading. To make the acquired hardness data reliable and reduce accidental errors, we adopt a 3 by 3 pattern (the gap between each other is 200 um) during testing. Finally, the unloading segment is analyzed by the designated software TriboScan Quasi for hardness computing. Here, the average brinell hardness of cured M-skin is ~ 144 MPa.

Analysis of the actuation ability of M-skin

The M-skin can provide magnetic force and torque for robot actuation under the external magnetic field. Assuming the single MP is a point-like dipole with a magnetic susceptibility χ under the magnetic field B, R is the diameter of the spherical MP. For a specific M-skin, N is the total contained MPs. Then, the endured magnetic force of M-skin can be expressed as: $F = N \bullet \frac{\pi R^3}{6} \bullet \chi \bullet \nabla B$. During which, the total number of MPs N and the external magnetic field gradient ∇B are adjustable, which determine the magnetic force, i.e. the magnetic force of M-skin is proportional to the MP mass fraction and applied magnetic field. Since the MPs inside the M-skin are aligned into magnetic chain during the curing process, the M-skin will endure magnetic torque until the magnetic field consists with the direction of magnetic chain. Assuming the magnetic chains are distributed evenly, d is the distance between inter particles, n is the number of the MPs in a single chain, α is the angle between the direction of magnetic field and magnetic chain. Then, the total magnetic torque of the M-skin can be expressed as *(29)*: $T = N\dfrac{4\mu_0 n\chi^2 R^6 \pi}{3d^3}B^2 \sin 2\alpha$. For a specific M-skin, n is proportional to N, and d is proportional to $\dfrac{1}{N}$, i.e. the magnetic torque of M-skin is proportional to the MP mass fraction, applied magnetic field B and the phase angle α.

Equipment and devices for magnetic field production

In our manuscript, two types of device/equipment, i.e., The Helmholtz coils and the portable permanent magnet, are employed to generate the magnetic field for different purposes. The Helmholtz coils system is adopted for magnetic related quantitative characterization when taking advantages of its precise magnetic strength and frequency. The permanent magnet is used for M-skin fabrication, reprogramming and robot actuation when taking benefits of its portable size. As shown in fig. S2C, the Helmholtz coils system includes three pairs of coils, with a size of 220 mm by 380 mm by 420 mm. And it can generate a magnetic field with max strength of 10 mT in the centre of workspace. As shown in fig. S2D, the permanent magnet is with a size of 50 mm by 50 mm by 25 mm and a max magnetic strength of 350 mT.

The permanent magnet model analysis

The magnetic field used for M-skin millirobots actuation is generated by the permanent magnet, where both the magnetic force and torque involve. For a rectangular permanent magnet, the magnetic induction intensity $\boldsymbol{B}$ on an arbitrary point can be described as

(36):

$$B_x = \frac{\mu_0 J_s}{8\pi}\Big[-\Gamma\left(0.5ml - x, 0.5mw - y, 0.5mh + z\right) - \Gamma\left(0.5ml - x, 0.5mw + y, 0.5mh + z\right) \\ + \Gamma\left(0.5ml + x, 0.5mw - y, 0.5mh + z\right) + \Gamma\left(0.5ml + x, 0.5mw + y, 0.5mh + z\right)\Big] \quad (1)$$

$$B_y = \frac{\mu_0 J_s}{8\pi}\Big[-\Gamma\left(0.5mw - y, 0.5ml - x, 0.5mh + z\right) - \Gamma\left(0.5mw - y, 0.5ml + x, 0.5mh + z\right) \\ + \Gamma\left(0.5mw + y, 0.5ml - x, 0.5mh + z\right) + \Gamma\left(0.5mw + y, 0.5ml + x, 0.5mh + z\right)\Big] \quad (2)$$

$$B_z = \frac{\mu_0 J_s}{4\pi}\Big[-\Psi\left(0.5mw - y, 0.5ml - x, 0.5mh + z\right) - \Psi\left(0.5mw + y, 0.5ml - x, 0.5mh + z\right) \\ - \Psi\left(0.5ml - x, 0.5mw - y, 0.5mh + z\right) - \Psi\left(0.5ml + x, 0.5mw - y, 0.5mh + z\right) \\ - \Psi\left(0.5mw - y, 0.5ml + x, 0.5mh + z\right) - \Psi\left(0.5mw + y, 0.5ml + x, 0.5mh + z\right) \\ - \Psi\left(0.5ml - x, 0.5mw + y, 0.5mh + z\right) - \Psi\left(0.5ml + x, 0.5mw + y, 0.5mh + z\right)\Big] \quad (3)$$

in which

$$\Gamma\left(\gamma_1, \gamma_2, \gamma_3\right) = \ln \frac{\sqrt{\gamma_1^2 + \gamma_2^2 + \left(\gamma_3 - z_0\right)^2} - \gamma_2}{\sqrt{\gamma_1^2 + \gamma_2^2 + \left(\gamma_3 - z_0\right)^2} + \gamma_2}\Bigg|_{z_0 = 0}^{z_0 = mh} \quad (4)$$

$$\Psi\left(\psi_1, \psi_2, \psi_3\right) = \arctan\left[\frac{\psi_1\left(\psi_3 - z_0\right)}{\psi_2\sqrt{\psi_1^2 + \psi_2^2 + \left(\psi_3 - z_0\right)^2}}\right]\Bigg|_{z_0 = 0}^{z_0 = mh} \quad (5)$$

where the coordinate (*x, y, z*) is the arbitrary point which out of the magnet and relative to the centre of magnet, B_x, B_y, B_z are the magnetic induction intensity along the *x*, *y* and *z* direction respectively, μ_0 is permeability of vacuum, J_s is the surface density of magnetizing current, and *ml, mw, mh* represent the length, width, height of the rectangular permanent magnet respectively.

The pulling force and torque force that M-skin millirobot experienced under magnetic field can be calculated as:

$$\vec{F} = V_R \cdot \left(\vec{M} \cdot \vec{\nabla}\right) \cdot \vec{B}\left(x, y, z\right) \quad (6)$$

$$\vec{T} = \int_{V_R} d\vec{T} dV = \int_{V_R} \left(\left(M_y B_z - M_z B_y\right)\vec{i} + \left(M_z B_x - M_x B_z\right)\vec{j} + \left(M_x B_y - M_y B_x\right)\vec{k}\right) dV \quad (7)$$

where $\vec{F}$ is the pulling force, $\vec{T}$ is the torque force, V_R is the volume of surface M-skin, $\vec{M}$ is the magnetization of M-skin and $\vec{B}(x,y,z)$ is magnetic flux intensity. Suppose the M-skin perpendicular to *xz* plane, θ is the angle between M-skin and *x* axis, when moving the permanent magnet forward along *x* axis, the pulling force and torque force along *x*, *y* and *z* axis can be respectively represented as:

$$\begin{cases} \vec{F}_x = \left(\cos\theta\dfrac{\partial B_x}{\partial x} + \sin\theta\dfrac{\partial B_z}{\partial x}\right)\displaystyle\int_{V_R} MdV \\ \vec{F}_y = \left(\cos\theta\dfrac{\partial B_x}{\partial y} + \sin\theta\dfrac{\partial B_z}{\partial y}\right)\displaystyle\int_{V_R} MdV \\ \vec{F}_z = \left(\cos\theta\dfrac{\partial B_x}{\partial z} + \sin\theta\dfrac{\partial B_z}{\partial z}\right)\displaystyle\int_{V_R} MdV \end{cases} \tag{8}$$

$$\begin{cases} \vec{T}_x = B_y \sin\theta \displaystyle\int_{V_R} MdV \\ \vec{T}_y = B_z \cos\theta \displaystyle\int_{V_R} MdV - B_x \sin\theta \displaystyle\int_{V_R} MdV \\ \vec{T}_z = -B_y \cos\theta \displaystyle\int_{V_R} MdV \end{cases} \tag{9}$$

In our embodiment, the size of the permanent magnet is 50 mm by 50 mm by 25 mm and located below the M-skin millirobot, the value of μ_0 is $4\pi \times 10^{-7}$ H/m, J_s is 3.1×10^4 A/m, the magnetic susceptibility of M-skin is measured by vibrating sample magnetometer (VSM) (DMS 1660, ADE Technologies).

<u>The motion criterion of constructed M-skin millirobot</u>

The M-skin millirobot with an irregular shape can be modelled as a piece of wrinkled paper which has *N* contacted lines with the ground and is composed of *M* parts hosted by M-spray. Here, we define the places where for M-spray pasting and beside the contact line as anchors, then the millirobot is divided into *M* parts according to the anchors. For the most common contact line c_n between M-skin millirobot and ground, it is an angle projection between i_{th} and $(i+1)_{\mathrm{th}}$ single anchor coated by M-spray on xz plane as shown in Fig. 3A.

For the i_{th} part beside the contact line, its dynamic model under magnetic field B is restricted on the xz plane and then can be established as follows:

$$m_i \ddot{x}_i = F_{xi} + {}^{i-1}_{i}F_x - {}^{i+1}_{i}F_x - F_{fn} \tag{10}$$

$$m_i \ddot{z}_i = F_{zi} + {}^{i+1}_{i}F_z + F_{Nn} - {}^{i-1}_{i}F_z - m_i g \tag{11}$$

$$J_i \ddot{\theta}_i = T_{y_i} + {}^{i-1}_{i}T_y - {}^{i+1}_{i}T_y - F_{fn} r_i \sin\theta_i + F_{Nn} r_i \cos\theta_i \tag{12}$$

in which,

$$F_{fn} = \mu(m_i g - F_{zi} + {}^{i-1}_{i}F_z - {}^{i+1}_{i}F_z) \tag{13}$$

where $r_i (i = 1, \ldots, N)$ is the distance between contact line c_n and mass centre m_i of the ith part, μ is friction coefficient, F_{Nn}, F_{fn} are supporting force and friction force from the ground, and T_{yi}, F_{xi}, F_{zi} are magnetic moment and drag forces along y axis, x axis, z axis, respectively. ${}^{i-1}_{i}T_y$, ${}^{i-1}_{i}F_x$, ${}^{i-1}_{i}F_z$ are equivalent moment and forces exerted by m_{i-1} part to m_i, and ${}^{i+1}_{i}T_y$, ${}^{i+1}_{i}F_x$, ${}^{i+1}_{i}F_z$ are equivalent moment and forces exerted by m_{i+1} part to m_i, respectively. Assuming there exists following inequations:

$$F_{xi} \neq \mu F_{Nn} + {}^{i+1}_{i}F_x - {}^{i-1}_{i}F_x \tag{14}$$

$$F_{zi} \neq {}^{i-1}_{i}F_z + m_i g - {}^{i+1}_{i}F_z - F_{Nn} \tag{15}$$

$$T_{yi} \neq (\mu \sin\theta_i - \cos\theta_i) F_{Nn} r_i + {}^{i+1}_{i}T_y - {}^{i-1}_{i}T_y \tag{16}$$

these dynamic characteristics can be obtained:

(1) $\ddot{x}_i \neq 0$ meaning it moves along x axis.

(2) $\ddot{z}_i \neq 0$ meaning it moves along z axis.

(3) $\ddot{\theta}_i \neq 0$ meaning it swings or rotates under the magnetic field.

For the single anchor with single M-skin (*i*=1), it can be mainly divided into plane, convex, concave and round based on the surface of target objects.

Definition: A single M-skin always exists that a parametrized continuous surface in $S \subset \mathbb{R}^3$ is a continuous map $\{\sigma: U \to \mathbb{R}^3\}$, where $U \subset \mathbb{R}^2$ non-empty set. Then there is a pair $(u,v) \in U$ as a set of coordinates of the point $\sigma(u,v)$ in the surface $S = \sigma(U)$, if the surface *S* is smooth, the components of $\sigma(u,v) = \{x(u,v), y(u,v), z(u,v)\}$ having continuous partial derivatives with respect to *u* and *v*, up to all orders.

The single M-skin can be generally established a continuously differential and bounded surface $S = \{(x,y,z) \in \mathbb{R}^3 | y = f(x,z)\}$. Considering contact status of M-skin millirobot with the ground, a projection of the surface *S* on *xz* plane can be simplified approximately to a quadratic curve *l* in $\mathbb{R}^2$

$$f(x,z) = a_0 x^2 + a_1 x + a_2(z) \tag{17}$$

where a_0, a_1 are constant real numbers, and $a_2(z) = \sum_{i=0}^{m} b_i z^{m-i} (0 \le m \le 2)$. In practice, the constructed M-skin millirobot always has at least a line or a part of the body contacting the ground. Hence, the projection curve *l* intersected with the ground, which is $f(x,0)$ =0 must have real solutions. According to the contacting status with the ground, we can generally classify the single cured M-spray (i=1) into three styles.

a) Plane style

When the target is of a plane object, the constructed M-skin millirobot is plane contact with the ground at the initial state. Similarly, the surface model of the plane M-skin millirobot is subject to constraint conditions $a_0 = b_0 = 0$, $a_1 \neq 0$, and $b_1 \neq 0$. In this case, the M-skin millirobot swings or rotates under the changing magnetic field and can be controlled to move by tumbling or slipping.

b) Concave or cylinder style

When the target is a concave object or cylinder, the constructed M-skin millirobot has one-point contact with the ground at the initial state. For the concave object, its projection curve is concave on *xy* plane and can be expressed by Equation (17) subject to $a_0 < 0$. Such single concave M-skin can be considered as two parts in the integrated dynamic model analysis and can swing or slip under magnetic actuating. In addition, for a cylinder target with a circular projection on *xy* plane, we can derive $b_2 = \frac{b_1^2}{4b_0} + \frac{a_1^2}{4a_0} - r^2$, $b_0 \neq 0$ and $a_0 \neq 0$ in equation (17). Such cylinder M-skin millirobot can be controlled to roll under the magnetic field.

c) Convex style

When the target is a convex surface, the constructed M-skin millirobot has two contact points with the ground at the initial state. For the surface model by equation (17), its feasible parameters satisfy $a_0 < 0$, $\frac{\partial^2 f}{\partial x^2} < 0$, $a_1^2 - 4a_0a_2 < 0$, $b_0 = 0$, and $b_2 \neq 0$. Similar to the concave surface, the single convex M-skin can also be divided into two parts in the integrated dynamic model analysis. In addition to the swing, the single convex M-skin millirobot can achieve walking by these two parts alternatively working as a supporting point.

Furthermore, the M-skin millirobot with a complex polyhedron which contains *N* contacted lines can be considered as an integrated system including *M* parts. Therefore, the integrated force of the complex M-skin millirobot meets:

$$\sum_{i=1}^{M} m_i \ddot{x}_i = \sum_{i=1}^{M} (F_{xi} + {}^{i-1}_{i}F_x - {}^{i+1}_{i}F_x) - \sum_{n=1}^{N} F_{fn} \tag{18}$$

$$\sum_{i=1}^{M} m_i \ddot{z}_i = \sum_{n=1}^{N} (F_{Nn}) + \sum_{i=1}^{M} (F_{zi} + {}^{i-1}_{i}F_z - {}^{i+1}_{i}F_z - m_i g) \tag{19}$$

$$\sum_{i=1}^{M} J_i \ddot{\theta}_i = \sum_{i=1}^{M} T_{y_i} + \sum_{i=1}^{M} ({}^{i-1}_{i}T_y - {}^{i+1}_{i}T_y) - \sum_{i=1}^{M} (\mu \sin\theta_i - \cos\theta_i)(m_i g - F_{zi} + {}^{i-1}_{i}F_z - {}^{i+1}_{i}F_z) r_i \tag{20}$$

subject to boundary conditions ${}^{0}_{1}F_x = {}^{0}_{1}F_z = 0$, ${}^{M+1}_{M}F_x = {}^{M+1}_{M}F_z = 0$, ${}^{0}_{1}T_y = {}^{M+1}_{M}T_y = 0$. Since these parameters ${}^{i-1}_{i}T_y$, ${}^{i-1}_{i}F_x$, ${}^{i-1}_{i}F_z$, ${}^{i+1}_{i}T_y$, ${}^{i+1}_{i}F_x$, ${}^{i+1}_{i}F_z$ are inner forces of the M-skin millirobot, the following conditions hold: ${}^{i-1}_{i}T_y = {}^{i}_{i-1}T_y$, ${}^{i-1}_{i}F_x = {}^{i}_{i-1}F_x$, ${}^{i-1}_{i}F_z = {}^{i}_{i-1}F_z$, $\sum_{i=1}^{M}({}^{i-1}_{i}F_x - {}^{i+1}_{i}F_x)=0$, $\sum_{i=1}^{M}({}^{i-1}_{i}F_z - {}^{i+1}_{i}F_z)=0$, and $\sum_{i=1}^{M}({}^{i-1}_{i}T_y - {}^{i+1}_{i}T_y)$. Hence, the above equations (18)-(20) can be furtherly derived as

$$F_x - F_f = \sum_{i=1}^{M} m_i \ddot{x}_i \tag{21}$$

$$F_z + F_N - Mg = \sum_{i=1}^{M} m_i \ddot{z}_i \tag{22}$$

$$\sum_{i=1}^{M} J_i \ddot{\theta}_i = T_y - \sum_{i=1}^{M} (\mu \sin\theta_i - \cos\theta_i)(m_i g - F_{zi}) r_i \tag{23}$$

where $\sum_{i=1}^{M} m_i = M$, $\sum_{i=1}^{M} F_{zi} = F_z$, $\sum_{n=1}^{N} F_{Nn} = F_N$, $\sum_{i=1}^{M} F_{xi} = F_x$, $\sum_{n=1}^{N} F_{fn} = F_f$, and $\sum_{i=1}^{M} T_{y_i} = T_y$.
The motion criterion of the single anchor and the integrated system can be used to guide the M-skin millirobot design. If there is an arbitrary value i that meets the inequality conditions $m_i \ddot{x}_i \neq 0, m_i \ddot{z}_i \neq 0$, or $J_i \ddot{\theta}_i \neq 0$, the constructed M-skin millirobot can response to the magnetic field.

<u>The analysis of soft reptile robot</u>

There are two states of the reptile robot (fig. S5C) during a walking circle: the line contact in the stretched state and two points contact in the curled state. When the magnet moving close and satisfy the motion criterion ($\ddot{\theta} > 0$), the two coated ends of robot tilting. Here, the horizontal force of parts *ab* and *cd* before slipping can be described:

$$\mu_1 \left[m_1 g + (\cos\theta_1 \frac{\partial B_x}{\partial Z} + \sin\theta_1 \frac{\partial B_z}{\partial Z}) \int_{V_1} M dV \right] = (\cos\theta_1 \frac{\partial B_x}{\partial x} + \sin\theta_1 \frac{\partial B_z}{\partial x}) \int_{V_1} M dV + {}^{2}_{1}F_x \tag{24}$$

$$\mu_2 \left[m_2 g + (\cos\theta_2 \frac{\partial B_x}{\partial Z} + \sin\theta_2 \frac{\partial B_z}{\partial Z}) \int_{V_2} M dV \right] = {}^{1}_{2}F_x - (\cos\theta_2 \frac{\partial B_x}{\partial x} + \sin\theta_2 \frac{\partial B_z}{\partial x}) \int_{V_2} M dV \tag{25}$$

where ${}_{1}^{2}F_{x}$ and ${}_{2}^{1}F_{x}$ are inner forces of robot, and they are equal. Since the friction coefficient is small enough, the maximum friction force of contact points *b* and *d* can be considered as same. Here the magnetic pulling forces are forward which do positive work to the part *ab* and do negative work to the part *cd*. Then, we can get that, as the increase of the inner force caused by magnetic torque in curling period, the contact point *b* will first break the balance state and slipped inward. For the stretched state, the situation reversed:

$$\mu_1\left[m_1 g+(\cos\theta_1\frac{\partial B_x}{\partial Z}+\sin\theta_1\frac{\partial B_z}{\partial Z})\int_{V_1} MdV\right]={}_{1}^{2}F_x-(\cos\theta_1\frac{\partial B_x}{\partial x}+\sin\theta_1\frac{\partial B_z}{\partial x})\int_{V_1} MdV \tag{26}$$

$$\mu_2\left[m_2 g+(\cos\theta_2\frac{\partial B_x}{\partial Z}+\sin\theta_2\frac{\partial B_z}{\partial Z})\int_{V_2} MdV\right]=(\cos\theta_2\frac{\partial B_x}{\partial x}+\sin\theta_2\frac{\partial B_z}{\partial x})\int_{V_2} MdV+{}_{2}^{1}F_x \tag{27}$$

The magnetic pulling forces do negative work to the part *ab* and do positive work to the part *cd*. That means the contact point *d* will slip forward in the stretched state rather than contact point *b*. Suppose the size of reptile robot before and after curled is S_1 and S_3 respectively, S_2 is the distance between the contact line and closer end, θ is the tilt angle. Then, the step size of reptile robot can be expressed as:

$$S_{Crawl}=(S_1-S_2)-(S_3-S_2\cos\theta_1)=S_1-S_3-(1-\cos\theta_1)S_2 \tag{28}$$

where S_1 and S_2 are related to the robot size. For a specific robot, the value of S_1 and S_2 are fixed. S_3 is the curled state size which decreases as the increase of both tilt angle θ_1 and θ_2. The tilt angle is depended on the applied torque of magnetic field T_y, the bending stiffness *E* and moment of inertia of cross-sectional area *I*.

$$\sin\theta\propto\frac{\mathrm{T}_y}{EI} \tag{29}$$

Based on this strategy, we assume the robot crawls under the magnetic field *B* with a frequency of f. Then, we can get the locomotion speed:

$$V_{Crawl} = S_{Crawl} f \tag{30}$$

Combine the equations (28)-(30), we can know the tilt angle θ_1, θ_2 and frequency f are the main factors of influence. For the specific size robot with the more flexible material, the stronger magnetic torque, the faster actuating frequency and the smaller cross-sectional area will have a longer step size and faster locomotion speed.

<u>The analysis of multi-foot origami robot</u>

As shown in fig. S5D, the direction of magnetic pulling force in *xy* plane has an angle α with one of four feet. When $0^\circ < \alpha < 90^\circ$ (the direction of magnetic pulling force F_{mi} within the $\angle bOd$), the force analysis of contact anchor feet along the diagonal direction before curling can be expressed as:

$$\begin{cases} \mu_a \left[m_a g + \sum\limits_a F_{mz} \right] = {}_a^O F + \cos\alpha_a \sum\limits_a F_{mi} \\ \mu_d \left[m_d g + \sum\limits_d F_{mz} \right] = {}_d^O F - \cos\alpha_d \sum\limits_d F_{mi} \end{cases} \tag{31}$$

$$\begin{cases} \mu_b \left[m_b g + \sum\limits_b F_{mz} \right] = {}_b^O F - \sin\alpha_b \sum\limits_b F_{mi} \\ \mu_c \left[m_c g + \sum\limits_c F_{mz} \right] = {}_c^O F + \sin\alpha_c \sum\limits_c F_{mi} \end{cases} \tag{32}$$

where ${}_a^O F$, ${}_d^O F$, ${}_b^O F$ and ${}_c^O F$ are inner force which caused by magnetic torque and along the diagonal, $\sum\limits_a F_{mz}$, $\sum\limits_b F_{mz}$, $\sum\limits_c F_{mz}$ and $\sum\limits_d F_{mz}$ are magnetic pulling force to anchor foot *a, b, c* and *d* along *z* direction. $\sum\limits_a F_{mi}$, $\sum\limits_b F_{mi}$, $\sum\limits_c F_{mi}$ and $\sum\limits_d F_{mi}$ are magnetic pulling force in XY plane to anchor foot *a*, *b*, *c* and *d* respectively, their angles with diagonal *aOd* are θ_a, θ_b, θ_c and θ_d which locate from 0° to 90°.

When the multi-foot origami robot stretching from curled state to relaxed state, the above equations can be derived as:

$$\begin{cases} \mu_a \left[m_a g + \sum_a F_{mz} \right] = {}_a^O F - \cos\alpha_a \sum_a F_{mi} \\ \mu_d \left[m_d g + \sum_d F_{mz} \right] = {}_d^O F + \cos\alpha_d \sum_d F_{mi} \end{cases} \tag{33}$$

$$\begin{cases} \mu_b \left[m_b g + \sum_b F_{mz} \right] = {}_b^O F + \sin\alpha_b \sum_b F_{mi} \\ \mu_c \left[m_c g + \sum_c F_{mz} \right] = {}_c^O F - \sin\alpha_c \sum_c F_{mi} \end{cases} \tag{34}$$

By combining the equations (31)-(34), we can get that the multi-foot origami robot first curled while taking the ends of foot *b* and *d* as anchors along diagonal direction respectively, then stretched while taking the ends of foot *a* and *c* as anchors along diagonal direction respectively. Here we assume each leg of robot has the same length S_1 before applying magnetic field and curls to S_2, S_3, S_4, S_5 respectively after applying magnetic field. The moving distance OO' of robot from relaxed state to curled state can be calculated by:

$$S_{Curl} = \sqrt{(S_1 - S_4)^2 + (S_1 - S_5)^2} \tag{35}$$

and the angle between the moving direction and *x* axis can be expressed by:

$$\beta_{Curl} = \frac{\pi}{4} - \arctan\frac{S_1 - S_4}{S_1 - S_5} \tag{36}$$

The moving distance $O'O''$ of robot from curled state to relaxed state can be calculated by:

$$S_{Stretch} = \sqrt{(S_1 - S_2)^2 + (S_1 - S_3)^2} \tag{37}$$

$$\beta_{Stretch} = \frac{\pi}{4} - \arctan\frac{S_1 - S_2}{S_1 - S_3} \tag{38}$$

when $\theta = 0^\circ$ or 90°, the magnetic pulling force along diagonal *bOc* ($\theta = 0^\circ$) or diagonal *aOd* ($\theta = 90^\circ$) becomes zero. That means the robot will walk along diagonal and the above equations can be derived as:

$$S_{Curl} = \begin{cases} S_1 - S_4 & (\beta = -\frac{\pi}{4}) \\ S_1 - S_5 & (\beta = \frac{\pi}{4}) \end{cases} \tag{39}$$

$$S_{Stretch} = \begin{cases} S_1 - S_2 & (\beta = -\frac{\pi}{4}) \\ S_1 - S_3 & (\beta = \frac{\pi}{4}) \end{cases} \tag{40}$$

We assume the multi-foot origami robot moves with the frequency *f* under the magnetic field *B*, then the locomotion speed of robot can be expressed as:

$$V_{Crawl} = S_{Crawl} f = \begin{cases} (2S_1 - S_2 - S_4) f & (\theta = 0^\circ) \\ \sqrt{(2S_1 - S_2 - S_4)^2 + (2S_1 - S_3 - S_5)^2} f & (0^\circ < \theta < 90^\circ) \\ (2S_1 - S_3 - S_5) f & (\theta = 90^\circ) \end{cases} \tag{41}$$

<u>The analysis of walking robot</u>

Despite the walking robot has different morphology from reptile robot, they have the same moving strategy. According to equations (24)-(27), the step size of the walking robot can be got:

$$S_{Walk} = 2(S_1 - S_2) \tag{42}$$

where S_1 and S_2 are the stretched and curled size respectively as shown in fig. S5E. We assume the robot can walk successfully with a frequency of f under the magnetic field *B*. Then it's walking speed can be expressed as:

$$V_{Walk} = S_{Walk} f = 2(S_1 - S_2) f \tag{43}$$

The analysis of rolling robot

Different from the robots discussed above, the rolling robot hardly changes its shape during the locomotion. Here the magnetic pulling force provides the actuating power, and the magnetic torque is mainly used for direction changing. The mechanical analysis of the rolling robot from the side view is shown in fig. S5F, and we can easily get the dynamic equation:

$$J\ddot{\theta} = F_f r_{eff} - C_R \dot{\theta} \tag{44}$$

where J and r_{eff} are the moment of inertia and radius of the rolling robot, $\ddot{\theta}$ and $\dot{\theta}$ are the angular acceleration and angular speed, C_R is the rotational damping coefficient. Assuming that the robot satisfies the no-slip condition when it rolls on the ground, then we can get:

$$F_f = F_{Mx} = \left(\sin\alpha \frac{\partial B_x}{\partial x} + \cos\alpha \frac{\partial B_z}{\partial x} \right) \int_{V_R} M dV \tag{45}$$

Substituting the equation (45) into equation (44), then the dynamic equation can be rewritten as:

$$J\ddot{\theta} = r_{eff} \left(\sin\alpha \frac{\partial B_x}{\partial x} + \cos\alpha \frac{\partial B_z}{\partial x} \right) \int_{V_R} M dV - C_R \dot{\theta} \tag{46}$$

That means the robot will roll when the horizontal magnetic pulling force is existing and exceeding the damping torque. And the robot will continue moving until locating directly above the magnet so that the rolling distance is always equal to the magnet moving distance. Since the continuous acceleration, the rolling robot always with a high velocity and finally stop by repeated oscillating beside the magnet.

Despite the M-spray winding into a ring, the net magnetic moment of rolling robot is always in the *xy* plane. For the net magnetic moment $\boldsymbol{M}$ with arbitrary direction, the generated magnetic torque force under $\boldsymbol{B}$ can be expressed:

$$\tau = \boldsymbol{M} \times \boldsymbol{B} \tag{47}$$

This equation implies that a magnetic torque will generate and act on robot as long as there is an angle between the $\boldsymbol{M}$ and $\boldsymbol{B}$. If no other torques are applying on the rolling robot, the generated magnetic torque will align the $\boldsymbol{M}$ of robot along the applied magnetic field $\boldsymbol{B}$. The above is the steering strategy we used to control the rolling direction of robot.

<u>The analysis of slipping robot</u>

The slipping motion of wooden stick is achieved by the cooperation of force and torque from the permanent magnet (fig. S5G). Once the pulling force exceeds the resistance force between robot, ground and air, the wooden stick will be imparted a high acceleration for moving forward. And the function of torque is rocking wooden stick during movement to adjust the friction force between robot and ground so that the controllable locomotion can be achieved. Suppose the permanent magnet forward and back along *x* axis, and the wooden stick moves in *xz* plane, we can develop the dynamic model:

$$m\ddot{x}_{COM} = F_{Mx} - F_f \tag{48}$$

$$m\ddot{z}_{COM} = F_N - F_{Mz} - mg \tag{49}$$

$$J_C\ddot{\theta} = T_M + F_f \frac{L}{2}\sin\theta - F_N \frac{L}{2}\cos\theta \tag{50}$$

where θ is the tilt angle between robot and *x* axis, $J_C = m\left(D^2 + L^2\right)/12 \approx mL^2/12$ is the polar moment of inertia of the robot, F_{Mx}, F_{Mz}, the pulling force of magnetic field along *x* and *z* axis, F_N, the supporting force from the ground, F_f, the force of friction, *mg* is the gravity of robot, T_M, magnetic moment, T_f, resistance torque. *D, L* are the diameter and length of the stick where *D* is far less than the *L*.

Suppose the initial coordinate of point P (P_x, P_y) that is a contact point between robot and ground, when the tilt angle between robot and *x* axis is within $0 \le \theta \le \frac{\pi}{2}$, we can get the position and acceleration of the COM of robot *(37)*:

$$x_{COM} = P_x + \frac{L}{2}\cos\theta \tag{51}$$

$$z_{COM} = P_z + \frac{L}{2}\sin\theta \tag{52}$$

$$\ddot{x}_{COM} = \ddot{P}_x - \frac{L}{2}\cdot\ddot{\theta}\cdot\sin\theta - \frac{L}{2}\cdot\dot{\theta}^2\cdot\cos\theta \tag{53}$$

$$\ddot{z}_{COM} = \ddot{P}_z + \frac{L}{2}\cdot\ddot{\theta}\cdot\cos\theta - \frac{L}{2}\cdot\dot{\theta}^2\cdot\sin\theta \tag{54}$$

By combining the equations (48)-(50) and (53)-(54), we have five equations and six unknown quantities $\left(\ddot{x}_{COM}, \ddot{z}_{COM}, \ddot{\theta}, \ddot{P}_x, \ddot{P}_z, F_f\right)$. To solve the under-defined system analytically, we first assume the contact point meets the pinned assumption, i.e. $\ddot{P}_x = 0$. If the solution shown $F_N < 0$ which means the contact point is not pinned, we should resolve the equations with $F_N = 0$, $F_f = 0$ and $\ddot{P}_x$ as an unknown. If the solution shown $F_f > F_{f\max}$ which also means the contact point is not pinned, we should resolve the equations with $F_f = F_{f\max}$ and $\ddot{\boldsymbol{P}}_x$ as an unknown. The acceleration solutions and corresponding time in one-time step can be used for calculating the velocity and position of robot. Then the determined position will be the initial state in the next step.

Evaluation of the motion ability on different substrate surfaces

To evaluate the locomotion performance of M-skin millirobots on diverse surface conditions, we test different locomotion modes including crawling, walking, rolling, slipping and flipping on the glass, ice, skin, wood and sand respectively. During which, the applied magnetic field with a max strength of ~ 50 mT and a max gradient ~ 1000 mT/m. The adopted surface, i.e., glass, ice, skin, wood and sand surfaces, are almost flat but with the different friction conditions. The motion performances on diverse surfaces are evaluated based on the robot's feasibility, stability, controllability as well as continuity, and classified into good, medium, poor (fig. S9 and table S1).

The disintegration of M-skin under different pH environment

The different pH environment (pH 1, 4, 7, 10, 13) is achieved by the combination of standard phosphatebuffer (pH 1-7) and 0.1% NaOH solution (pH ~13). The real pH of the obtained environmental solution is ensured and detected by a pH meter (INESA (Group) Co. Ltd.). The M-skin with the same size of 5 mm by 5 mm and material components is soaked under the different pH environment. The swelling and disintegration time of M-skin without magnetic oscillation (Fig. 5F, fig. S14, tables S2 and S3), as well as the disintegration rate of M-skin with magnetic oscillation (Fig.5G), are all recorded. The oscillating magnetic field with a strength of 10 mT and a frequency of 1 Hz is applied by Helmholtz coils system. The disintegration rate is calculated as the ratio between the area of fragmentations and the origin area of M-skin. And the fragmentations with the size that smaller than 2.5% of origin area are considered as disintegrated.

Evaluation of reprogramming stability and repeatability

In practice, a mass fraction of 40% MP is used to construct the M-skin. However, in this case, it's hard to see the reorganization of MP chains from the image during reprogramming due to the mutual coverage of excessive MPs. To intuitively show the reorganization process of the easy magnetization axis, we use a low MP mass fraction 1% for demonstration in Fig. 4B and supporting video. The magnetic chains inside the M-skin (MP mass fraction 1%) are initially aligned and fixed along the horizontal. Then we wet it fully and apply an external 200 mT magnetic field perpendicular to the initial magnetization direction. The reorganization process of the magnetic chains in 10 min is recoded (movie S4).

To evaluate the stability and repeatability of reprogramming, the M-skin with MP content of 40%, a size of 5 mm × 5 mm is taken for test. The easy magnetization axis direction state with different programming magnetic field and time (Fig. 4C) is detected by observing the final stable direction of the free sample under the directional magnetic field. For the quantitative magnetization measurement of M-skin before and after reprogramming (Fig. 4D), the sample is fixed on substrate and keep its easy magnetization axis along the horizontal direction. Then, the sample is thoroughly wetted by splashing water on it. After that, the magnetic field with a strength of 200 mT is applied perpendicularly to the initial easy magnetization axis to reprogram the M-skin with 10 min. The magnetization before and after reprogramming is measured by VSM (DMS 1660, ADE Technologies).

Topology order reprogramming of M-skin millirobot

The transform between 3-D caterpillar and 2-D concertina motion is achieved by reprogramming the easy magnetization axis of M-skin. At initial, the M-spray is coated to the three coated parts of the plastic belt and magnetized along its long axis by applying a 100 mT magnetic field before curing to construct the 3-D caterpillar millirobot. When the 2-D concertina motion is needed, we can reprogram the easy magnetization axis of M-skin under the fully wetted condition. In this reprogramming demonstration, we fix the robot and apply the magnetic field 200 mT to re-align the orientation of the easy magnetization axis along diagonal. As the PVA turns into the swelling state by fully wetting, the constraint to the MPs greatly reduces, and they are reorganized under the action of magnetic torque. After excess water evaporates, the reprogramming of cured M-skin's easy magnetization axis is completed. Note that if the M-skin millirobot is not fixed, the millirobot will response to the magnetic field as a whole, and the magnetic chain cannot change its initial alignment orientation.

The analysis of 3-D caterpillar and 2-D concertina motion

The reptile millirobot with three sections can perform both 3-D caterpillar and 2-D concertina motion by reprogramming easy magnetization axis while keeping the main structure unchanged. Although the caterpillar and concertina motion show different characteristics, they are both belong to the reptile motion and can be analyzed as soft reptile robot. Initially, the easy magnetization axes of these three M-skins are aligned along horizontal, and they will tilt up or down following the magnetic field with an average angle of 47.3°, 52.3°, 67.7° respectively. During which, the robot crawls forward ~4.4 mm by alternating the front anchor and rear anchor like a caterpillar. When the easy magnetization axes of these three M-skins are reprogrammed along the diagonal, the robot can shrink to "S" form under a horizontal magnetic field and restore by removing the magnetic field. During which, three M-skins rotate with an average angle of 20.8°, 18.9°, 27.1° respectively and the robot will deform like a concertina to move forward ~0.5 mm by alternating anchors. The locomotion distance comparison under the same magnetic field with a frequency of 1 Hz indicates the caterpillar motion allows the robot to move more efficiently in free space which is almost 10 times the concertina motion (Fig. 4G). While the robot height variation is from 0.4 to 4.7 mm during caterpillar motion and from 0.4 to 1.5 mm during concertina motion, which means concertina motion allows the robot to cling on the ground when crossing the narrow space (Fig. 4H).

Influence of blood flow on the motion and disintegration of the catheter

We prepare a catheter with a total length of 100 mm, a diameter of 1 mm, and cover its tip by M-spray with a length of 8 mm and a thickness of ~150 μm. Then, we insert the catheter in a pipe (diameter 5 mm) containing 0.12% alginate solution with a viscosity of 3-4 mPa·s (similar as blood). A peristaltic pump is employed to make the solution flow at various speed to simulate the blood flow in blood vessel. For the actuation, a magnetic field with gradient ~ 1 T/m is applied, and the movement speed of catheter under different flow speed is recorded (fig. S15D). Despite the average speed of catheter decreases as the increase of liquid flow velocity, the catheter can be actuated even when the flow velocity reaches 200 mm/s which is large than the blood velocity in human vena (~150 mm/s). For investigating the disintegration of M-skin from the catheter, we first test its disintegration under the action of liquid flow. Then, applying an oscillating magnetic field (10 mT, 1 Hz) to investigate the disintegration under the action of both liquid flow and magnetic oscillation (fig. S15E). When the oscillating magnetic field is applied, the M-skin can disintegrate quickly within 6 min. Yet, without oscillating magnetic field, the M-skin can keep stable for 50 to 20 min as the liquid flow velocity changes from 50 to 200 mm/s.

The construction of the multi-point M-skin cotton thread

The cotton thread with a diameter of 2.5 mm is taken as the substrate, and the M-spray is coated to form three M-skin sections on it. During which, each M-skin section with a length of 5 mm and a gap of 2.5 mm. The magnetic field with a strength of 200 mT is adopted to program the easy magnetization axis of each section on demand. After the curing process, we can obtain the designed multi-point M-skin cotton thread.

The drug delivery demonstration in ex vivo pig stomach

The real pig stomach is obtained from the market. The viscosity of the gastric juice on the surface is detected by the rotational viscometer (NDJ-5S, Guangzhou Keyu Instruments Co. Ltd.), which is about 400 mPa·s and the pH is tested by the pH meter (INESA (Group) Co. Ltd.) which is about 5.5. During actuation, the magnetic field with a strength of ~50 mT and a gradient of ~1000mT/m is applied by permanent magnet. The buffer solution with a pH of 5.5 is adopted to simulate the liquid environment for robot disintegration and drug release.

The calculation of actual generated magnetic force and torque

Since the magnetization of M-skin can be measured by the VSM and its volume can be estimated according to the shape as well as size, the generated magnetic force and torque can be calculated. For the M-skin with 40% MP mass fraction, its magnetization *M* under 50 mT magnetic field is about 70.6 kA/m. The volume of M-skin on the catheter can be expressed as:

$$V_{c1} = \pi L\left[(\frac{D}{2} + \Delta d_1)^2 - (\frac{D}{2})^2 \right] \tag{55}$$

where L = 8 mm is the length of M-skin section, D = 1 mm is the diameter of catheter, Δd_1 = 0.15 mm is the average thickness of M-skin on catheter. While the volume of M-skin on the capsule can be expressed as:

$$V_{c2} = \frac{4}{3}\pi\left[(r_1 + \Delta d_2)^2(r_2 + \Delta d_2) - r_1^2 r_2\right] \tag{56}$$

where r_1 = 4 mm and r_2 = 7 mm are the short and long axis of the ellipsoidal capsule respectively, Δd_2 = 0.10 mm is the average thickness of M-skin on capsule. Then, the maximum generated magnetic force and torque of M-skin catheter as well as M-skin capsule under the magnetic field (strength 50 mT and gradient 1000 mT/m) can be calculated by substituting those value into the equation (6) and (7):

$$F_{catheter} = V_{c1} \bullet M \bullet \nabla B = 0.3 \ \text{mN} \tag{57}$$

$$T_{catheter} = V_{c1} \bullet M \bullet B \bullet \sin(\frac{\pi}{2}) = 1.5 \times 10^{-5} \ \text{N} \cdot \text{m} \tag{58}$$

$$F_{capsule} = V_{c2} \bullet M \bullet \nabla B = 2.2 \ \text{mN} \tag{59}$$

$$T_{capsule} = V_{c2} \bullet M \bullet B \bullet \sin(\frac{\pi}{2}) = 1.1 \times 10^{-3} \ \text{N} \cdot \text{m} \tag{60}$$

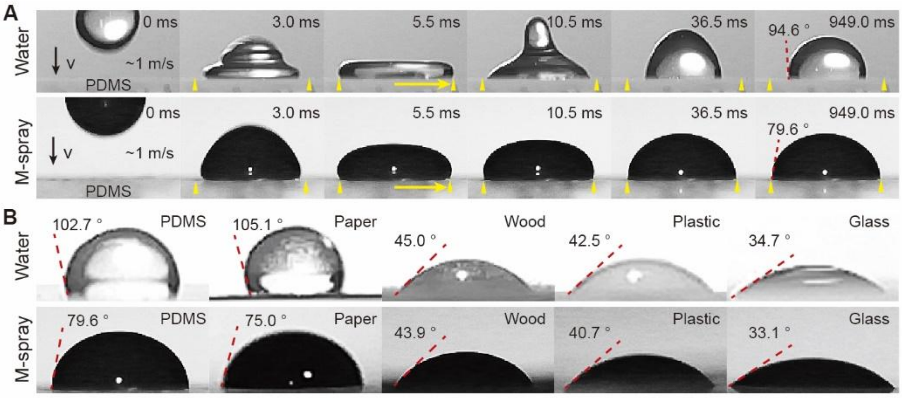

Fig. S1. The comparison of adhesion property between water droplet and M-spray droplet. A, The phenomena of bounce is observed in the water droplet landing process, and the corresponding radius of the contact area increases first then decreases. While the M-spray droplet adheres to the substrate immediately and the radius of the contact area never decreases. **B,** The static contact angle of water droplet on different materials which indicates the hydrophobicity/philicity of surface, and the final contact angle of M-spray that be coated to the corresponding target surface.

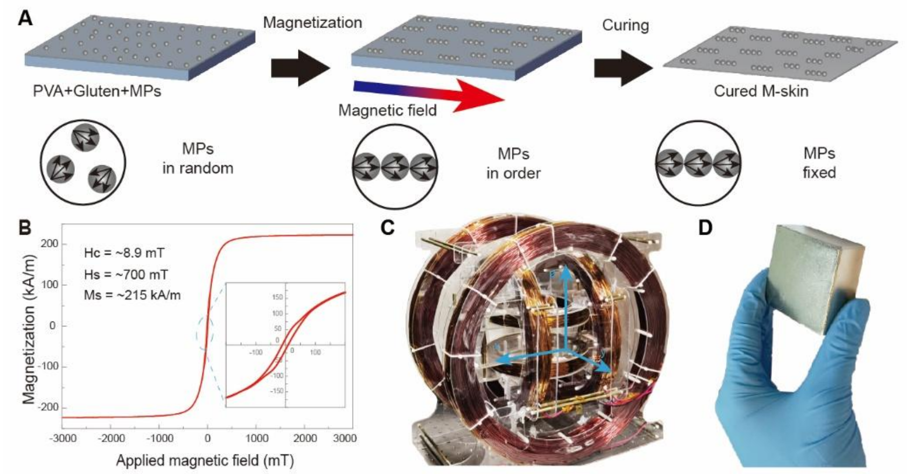

Fig. S2. The curing process and magnetic property of M-spray and the equipment used for magnetic field production. A, At initial, the M-spray is coated on the target surface, and the inside MPs are randomly distributed. Under the uniform magnetic field, MPs in the colloidal-liked film are aligned along magnetic field line and fixed with thermal curing. Finally, the easy magnetization axis orientated M-skin can be obtained. **B,** The hysteresis loop of M-skin. **C,** The Helmholtz coils system used for the magnetic related quantitative characterization including three pairs of coils in *x*, *y* and *z* direction. Each coil is driven independently by a servo amplifier, and the max magnetic field strength generated in the centre of workspace is 10 mT. **D,** The portable and powerful permanent magnet with a max magnetic strength of 350 mT.

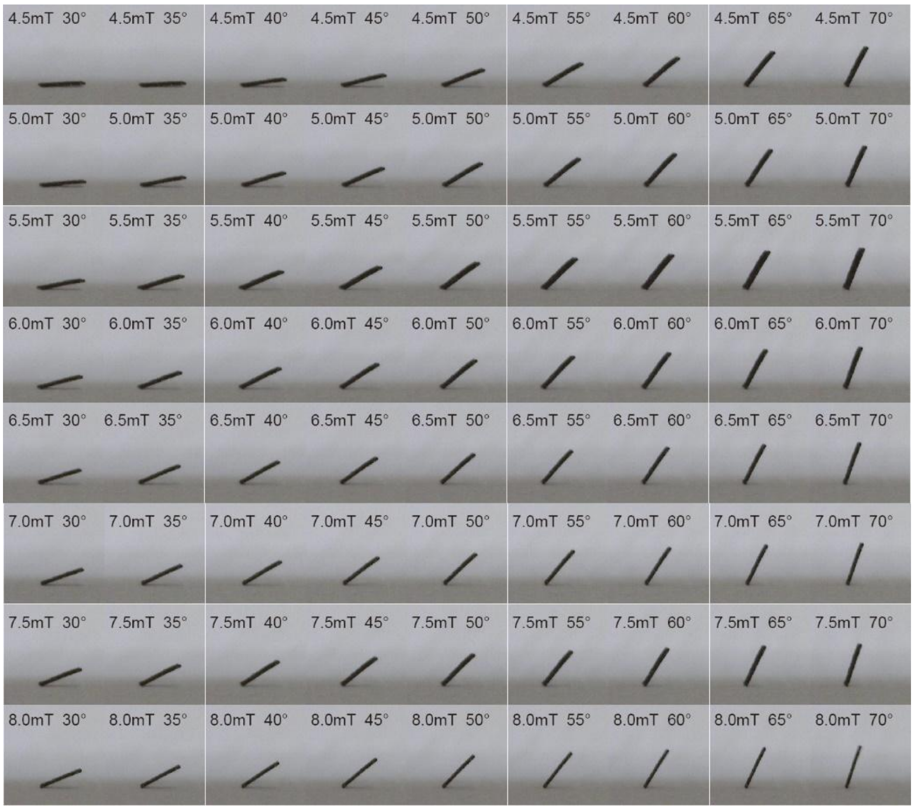

Fig. S3. Actuating performance of the M-skin under magnetic field. The tilt angle of M-skin under uniform magnetic field which strength changes from 4.5 to 8.0 mT and the inclination changes from 30 to 70°. Here, the tilt angle reflects the actuating torque of magnetic field and the results indicate that the larger magnetic strength or larger angle between the M-skin and magnetic field, the larger actuating torque. In this embodiment, the M-skin with a magnetic content of 40% and a size of 2 mm by 3 mm. The applied uniform magnetic field is generated by Helmholtz coils system.

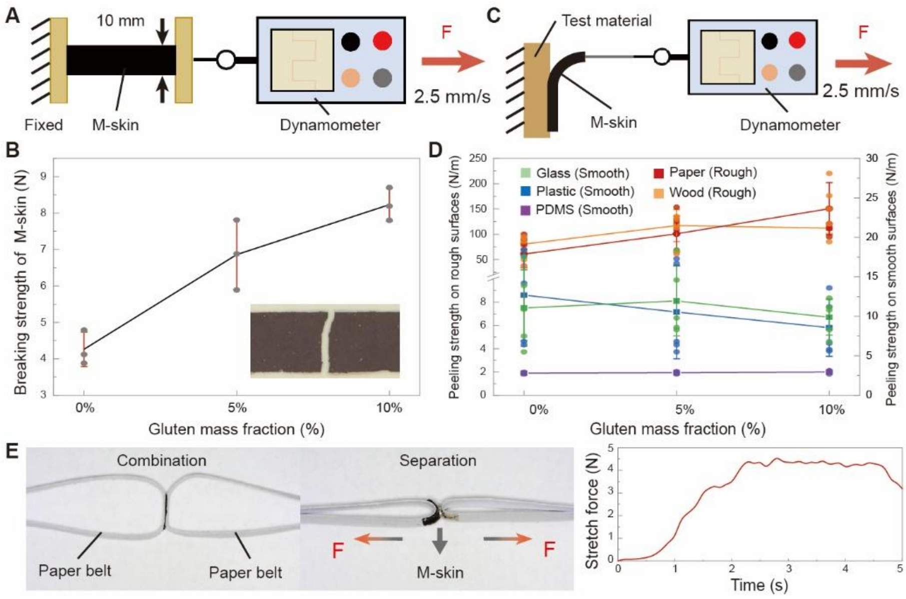

Fig. S4. Mechanical properties and adhesiveness of the cured M-spray. A, The schematic diagram of the breaking strength measurement. The one end of the strip sample (10 mm width) is fixed, and the dynamometer pulls the other end for recording the max breaking strength. **B,** The effects of gluten mass fraction on breaking strength. The generated network structure of gluten can enhance the mechanical properties of cured M-spray. Error bars indicate the SD for n=3. **C,** The schematic diagram of the peeling strength measurement. The M-spray is coated to testing materials with a width of 25 mm. Then, peel off the cured M-spray with dynamometer along the long axis direction and vertical to the surface with a speed of 2.5 mm/s. **D,** The effects of gluten mass fraction on peeling strength. The addition of gluten can slightly enhance the peeling strength of cured M-spray on the rough surface but hardly work on the smooth surface. Error bars indicate the SD for n=10. **E,** The M-spray is able to bond the paper belts together with an adhesion strength of ~0.17 N/mm^2 after curing.

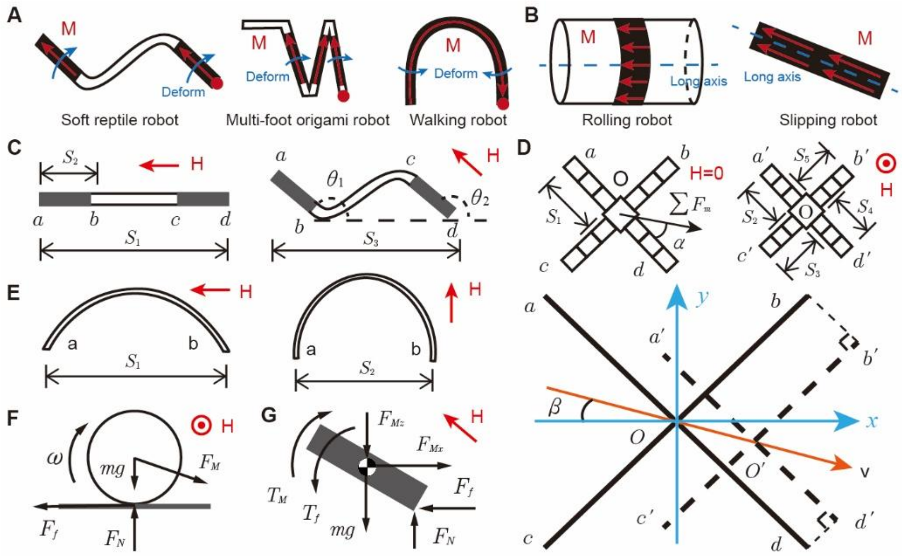

Fig. S5. The design and locomotion analysis of diverse M-skin millirobots. A, The principle of turning deformable inanimate objects into millirobots. Here, we magnetize the surficial M-skin perpendicularly to the deformation direction to achieve a repeatable morphological change. **B,** The principle of turning rigid inanimate objects into millirobots. Here, we magnetize the M-skin parallelly to its long axis to achieve movement as a whole, such as slipping, flipping and rolling. **C,** The state of soft reptile robot defined by several parameters and corresponding magnetic field during a walking cycle. **D,** The state of multi-foot origami robot defined by several parameters and corresponding magnetic field during a walking cycle. **E,** The state of walking robot defined by several parameters and corresponding magnetic field during a walking cycle. **F,** The mechanical analysis of rolling robot under magnetic field. **G,** The mechanical analysis of slipping robot under magnetic field.

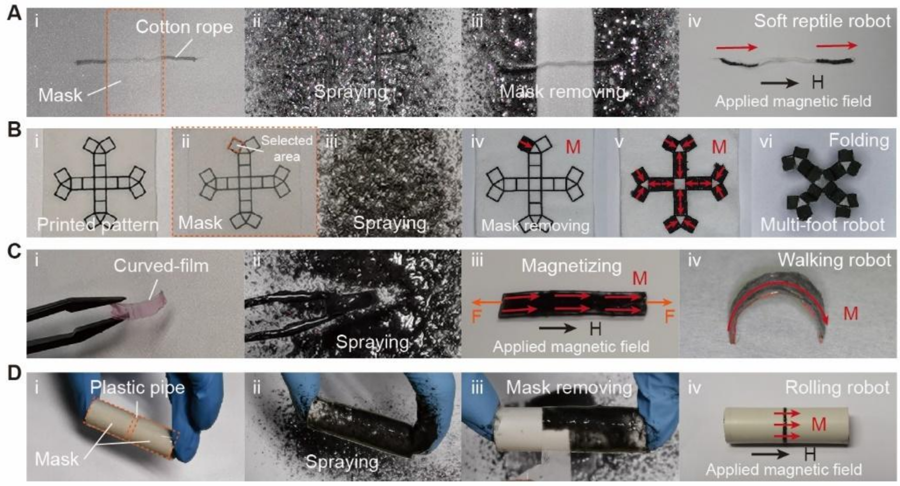

Fig. S6. The construction process of M-skin millirobots. A, The construction process of soft reptile robot, which is partly coated and with single magnetization direction, a mask is needed to protect the unselected region during the coating. **B,** The construction process of multi-foot origami robot, which is multi-partially coated and with multiple magnetization directions, is the most complex and difficult. **C,** For the walking robot, which is fully coated and with single magnetization direction, the manufacturing process is the simplest. **D,** The construction process of rolling robot, which is also partly coated and with single magnetization direction.

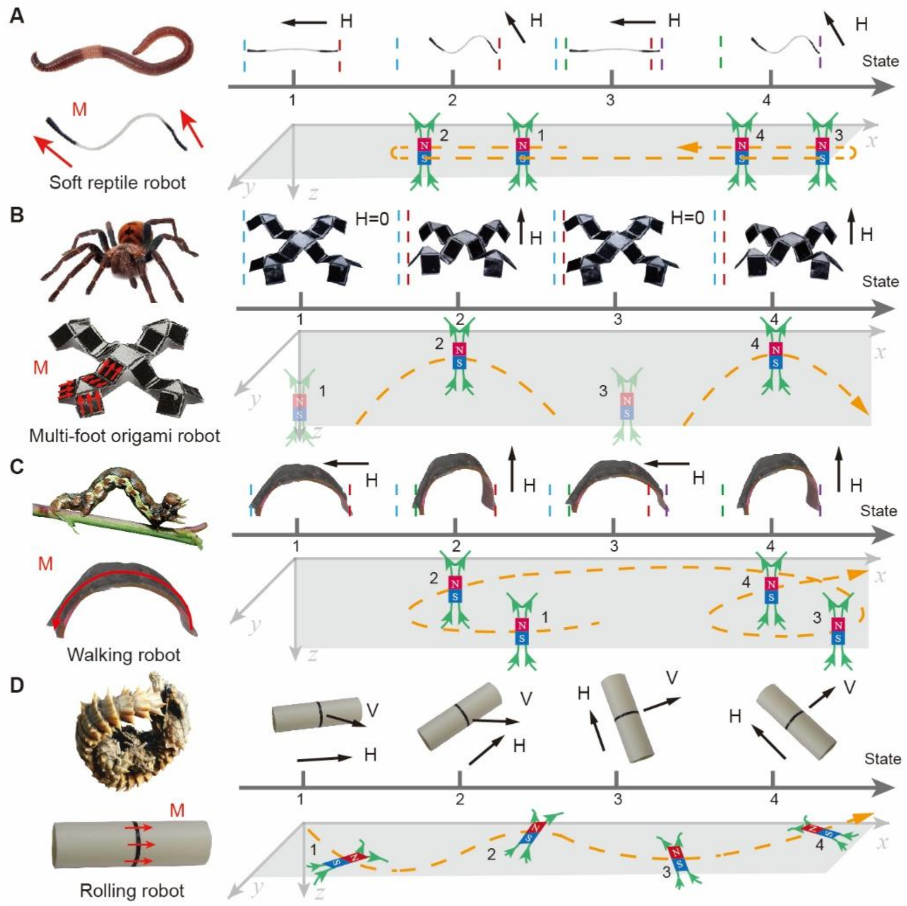

Fig. S7. The actuation of M-skin millirobots by permanent magnet. A, For the soft reptile robot, the swing magnetic field is generated by the reciprocating motion of permanent magnet in the "*xy*" plane. **B,** For the multi-foot origami robot, the locomotion is achieved by moving permanent magnet upper and down in the "*yz*" plane to simulate the ON and OFF mode of magnetic field. **C,** For the walking robot, the locomotion is achieved by moving permanent magnet in the "*yz*" plane with an "O" trajectory. **D,** For the rolling robot which cannot deform shape, the magnetic pulling force provides the power for rolling, and the magnetic torque force controls the movement direction.

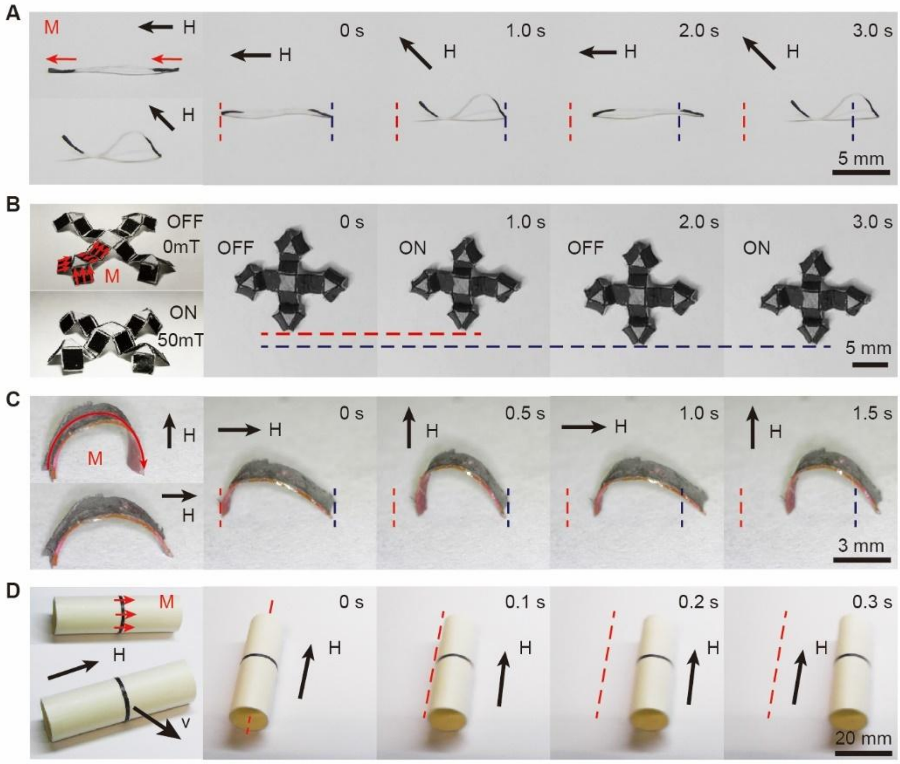

Fig. S8. Locomotion demonstration of the constructed M-skin millirobots. A, The easy magnetization axis direction of M-skin in the constructed soft reptile robot and corresponding creeping motion under magnetic field. **B,** The easy magnetization axis direction of M-skin in the constructed multi-foot origami robot and corresponding crawling motion under magnetic field., **C,** The easy magnetization axis direction of M-skin in the constructed walking robot and corresponding walking motion under magnetic field. **D,** The easy magnetization axis direction of M-skin in the constructed rolling robot and corresponding rolling motion under magnetic field.

Fig. S9. The performance evaluation of different motion modes on diverse surfaces. The crawling, walking, rolling, slipping and flipping motion are tested on the different surface conditions including glass, ice, skin, wood as well as sand. The corresponding motion performances are evaluated into good, medium, poor from the feasibility, stability, controllability as well as continuity. The results correspond to table S1.

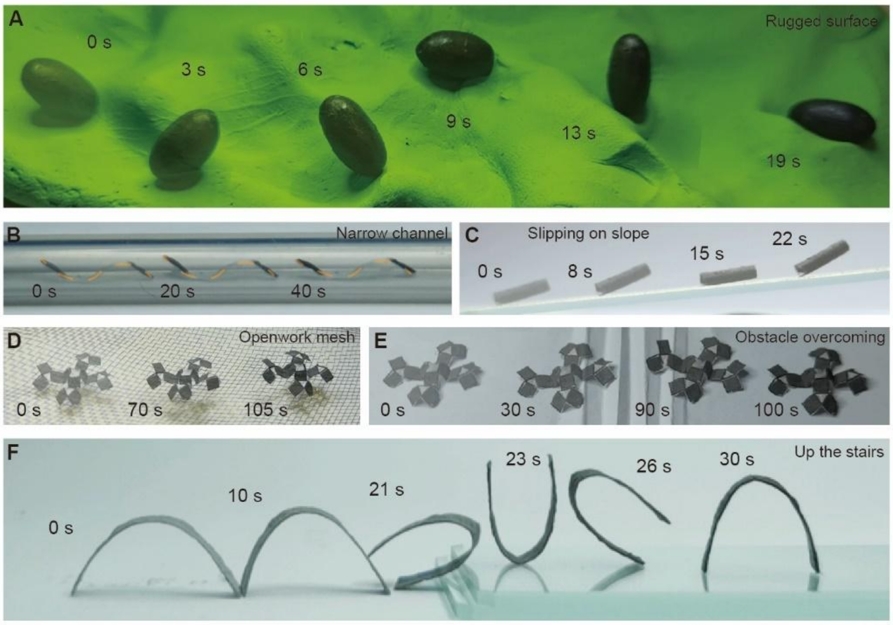

Fig. S10. The environment adaptability and obstacle overcoming ability of diverse M-skin millirobots. A, Optical images show the M-skin capsule can cross the rugged surface by flipping motion. **B,** The constructed reptile robot can perform excellently in the narrow channel due to its small size and flexible body. **C,** The slipping movement still works even on the slope. **D,** The multi-foot origami robot can crawl on the openwork mesh, just like the spider walking on the web. **E,** The obstacle overcoming demonstration of multi-foot origami robot. **F,** The curved-film walking robot can walk on the flat surface, and flip as a whole for going up the stairs.

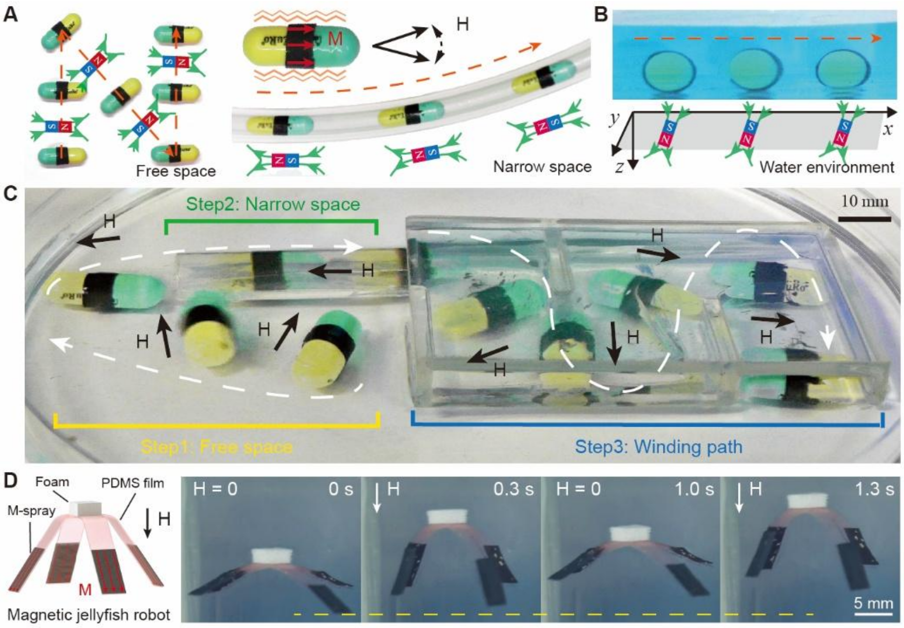

Fig. S11. The constructed M-skin millirobots work in both land and liquid environment. A, Photographs showing the constructed M-skin capsule works in the dry environment including free space and narrow space. **B,** The constructed M-skin capsule can still work even in the water environment. **C,** The controllable locomotion demonstration of M-skin capsule underwater. In this underwater demo, the M-skin capsule starts from a free space then crosses a narrow pipe to escape the maze at the end. **D,** The magnetic jellyfish robot constructed by M-spray can swim forward in the liquid media.

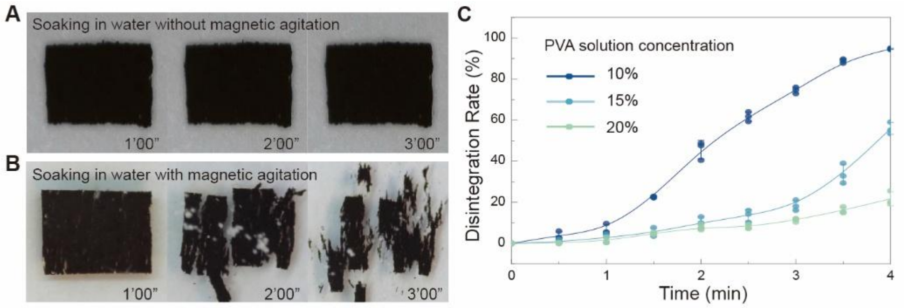

Fig. S12. Controllable magnetic-induced disintegration of M-skin in aquatic environment. A, The disintegration rate of M-skin as time without magnetic agitation in the aquatic environment. **B,** The disintegration rate of M-skin as time with magnetic agitation in the aquatic environment. **C,** The disintegration rate of M-skin as time when the adopted PVA solution concentration changes from 10 to 20% and keep the gluten content at 5%. During which, the M-skin size is about 5 mm by 5 mm, the applied magnetic field with a strength of 10 mT and a frequency of 1 Hz. Error bars indicate the SD for n=3.

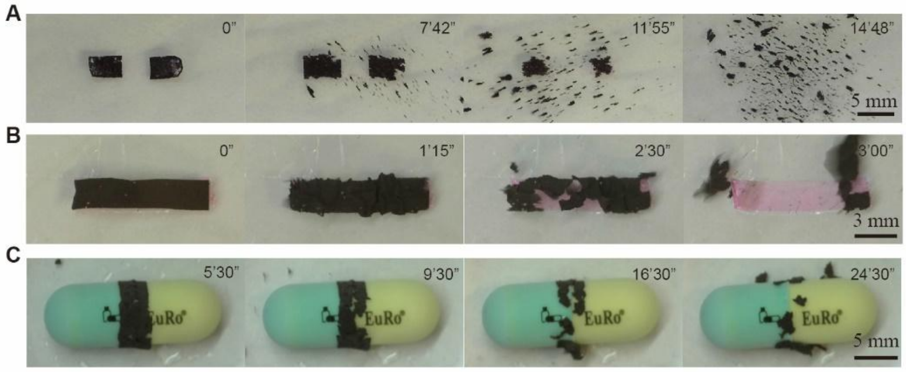

Fig. S13. The process that M-skin detaches after task completing from target inanimate objects. A, The disintegration of M-skin from PDMS-based reptile robot in the aquatic environment. **B,** The disintegration of M-skin from walking robot in the aquatic environment. **C,** The disintegration of M-skin from capsule robot in the aquatic environment. During which, the applied oscillating magnetic field with a strength of 10 mT and a frequency of 1 Hz.

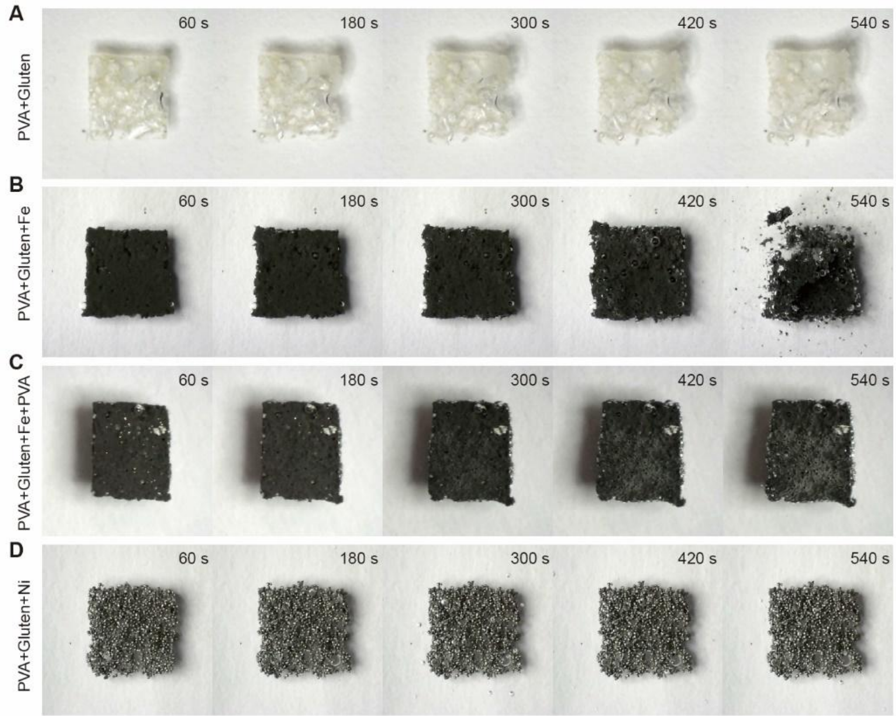

Fig. S14. The disintegration of M-skin with different material components in strong acid environment (pH 1) without magnetic oscillation. A, The M-skin without MPs can keep stable even in the strong acid environment. **B,** Due to the chemical reaction between iron particles inside the M-skin and the hydrogen ions inside the strong acid environment, the M-skin will start to disintegrate in about 8 min even without magnetic oscillation. **C,** By coating an additional PVA layer on the surface of M-skin after curing, the disintegration process can extend to about 15 min. **D,** M-skin with nickel particles instead of iron particles can keep stable in the strong acid environment.

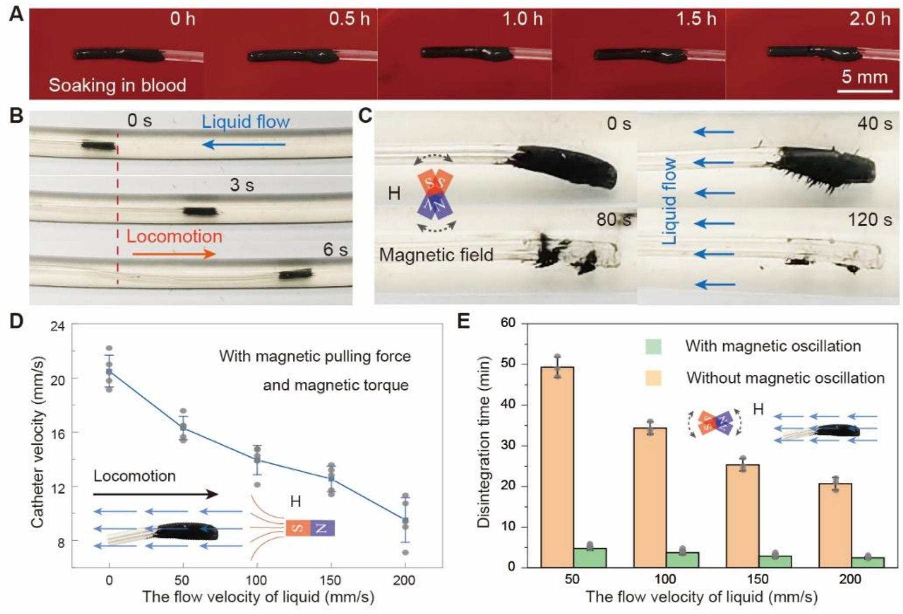

Fig. S15. The influence of physiological blood flow on the locomotion speed and disintegration process of M-skin catheter. A, The stability of M-skin catheter when soaking in the still blood. **B,** The locomotion of M-skin catheter against the liquid flow. **C,** The disintegration of M-skin from catheter under the action of both fluid flushing and magnetic oscillation. **D,** The motion speed change of catheter when the liquid flow velocity increases from 0 to 200 mm/s. Error bars indicate the SD for n=5. **E,** the disintegration of M-skin from catheter under the action of fluid flushing. Error bars indicate the SD for n=3.

Table S1. The performance evaluation summary of different motion modes under diverse surface conditions

Locomotion mode	Motion performance evaluation				
	Glass	**Ice**	**Skin**	**Wood**	**Sand**
Reptile crawling	Medium	Medium	Good	Medium	Medium
Multi-foot crawling	Medium	Medium	Good	Good	Good
Curved-film walking	Good	Good	Medium	Medium	Poor
Pipe rolling	Medium	Poor	Good	Good	Good
Stick slipping	Medium	Medium	Medium	Poor	Poor
Capsule flipping	Medium	Medium	Good	Good	Good

Table S2. The swelling and disintegration of M-skin without magnetic oscillation under different environmental temperature and pH

Temperature (℃)	State	Time (s)				
		pH 1	pH 4	pH 7	pH 10	pH 13
Room temperature (20 ℃)	Full swelling	320±26	394±48	431±52	485±33	666±50
	Disintegration	1480±183	4480±703	6260±600	8700±950	Never
Body temperature (37 ℃)	Full swelling	148±18	311±31	376±36	422±36	467±43
	Disintegration	620±91	3040±682	4820±330	6386±388	10400±916

Table S3. The swelling and disintegration time of cured film composed of different materials without magnetic oscillation

Material composition	**State**	**Time (s)**				
		pH 1	**pH 4**	**PH 7**	**pH 10**	**pH 13**
PVA solution	Full swelling	168±39	256±50	350±38	416±85	477±48
	Disintegration	3500±641	4486±280	5386±1120	7560±1101	Never
40% Fe in PVA solution	Full swelling	93±20	199±50	266±44	315±33	358±13
	Disintegration	760±124	3040±307	4300±283	5780±510	Never
40% Fe and 10% gluten in PVA solution	Full swelling	320±26	394±48	431±52	485±33	666±50
	Disintegration	1480±183	4480±703	6260±600	8700±950	Never

Table S4. Substrates used in the M-skin disintegration testing

Materials	**Size (mm^3)**	**Weight (g)**	**Remarks**
Wood	10 × 10 × 5.0	0.4643	Cedar
Paper	10 × 10 × 0.1	0.0085	A4 paper
PDMS	10 × 10 × 0.7	0.0632	0.1 equivalent curing agents
Glass	10 × 10 × 1.0	0.2681	CAT.NO.7107, Sail brand
Plastic	10 × 10 × 0.3	0.0323	Polyethylene

Supplementary movies

Movie S1. Coating of the M-spray droplet on target surfaces.

Movie S2. M-spray–enabled M-skin millirobots.

Movie S3. The environment adaptability of constructed M-skin millirobots.

Movie S4. Topology order reprogramming of the M-skin millirobot.

Movie S5. Magnetic-induced disintegration.

Movie S6. M-skin–covered catheter for active navigating.

Movie S7. M-skin–covered capsule for target drug delivery.